HHS Public Access

Author manuscript

IEEE Trans Biomed Eng. Author manuscript; available in PMC 2023 November 01.

Published in final edited form as:

IEEE Trans Biomed Eng. 2022 November ; 69(11): 3551–3558. doi:10.1109/TBME.2022.3174847.

Characterizing spatial signatures of gastric electrical activity using biomagnetic source localization

Recep Avci,
Auckland Bioengineering Institute, University of Auckland, New Zealand.

Chad E. Eichler,
Auckland Bioengineering Institute, University of Auckland, New Zealand.

Niranchan Paskaranandavadivel,
Auckland Bioengineering Institute, University of Auckland, New Zealand.

Peng Du,
Auckland Bioengineering Institute, University of Auckland, New Zealand.

Timothy R. Angeli-Gordon,
Auckland Bioengineering Institute, University of Auckland, New Zealand.

Leonard A. Bradshaw,
Department of Surgery, Vanderbilt University, TN, USA.

Leo K. Cheng
Auckland Bioengineering Institute, University of Auckland, New Zealand.; Department of Surgery, Vanderbilt University, TN, USA.

Abstract

Background: The motility patterns in the gastrointestinal tract are regulated, in part, by bioelectrical events known as slow waves. Understanding temporal and spatial features of gastric slow waves can help reveal the underlying causes of functional motility disorders.

Objective: This study investigated the ability of source localization techniques to characterize the spatial signatures of gastric slow wave activity using simulated and experimental magnetogastrography data.

Methods: Two slow wave propagation patterns (antegrade and retrograde) with two rhythms (normogastric and bradygastric) were used to simulate far-field magnetic fields using 4 anatomically realistic stomach and torso geometries. Source localization was performed utilizing the equivalent current dipole (ECD) and the equivalent magnetic dipole (EMD) models.

Results: In the normogastric simulations when compared with the underlying slow wave activity, the EMD model was capable of identifying the slow wave propagation in the lateral, antero-posterior, and supero-inferior directions with the median correlation coefficients of 0.66, 0.53, and 0.83, respectively, whereas the ECD model produced lower correlation scores (median: 0.52, 0.44, and 0.44). Moreover, the EMD model resulted in distinct and opposite spatial signatures

recep.avci@auckland.ac.nz.

for the antegrade and retrograde propagation. Similarly, when experimental data was used, the EMD model revealed normal antegrade-like spatial signatures where most of the propagation was towards the third quadrant in the supero-inferior (preprandial: 49%, postprandial: 35%) and antero-posterior (preprandial: 49%, postprandial: 50%) axes.

Conclusion and Significance: The EMD model was able to identify and classify the spatial signatures of slow wave activities. It can help to inform the interpretation of non-invasive recordings of gastric slow waves as a biomarker of functional motility disorders.

Keywords

Slow waves; magnetogastrography; source localization; functional gastric motility disorders

I. Introduction

The digestive process of the gastrointestinal (GI) tract is reliant on coordinated motility patterns regulated by the enteric nervous system and bioelectrical events known as slow waves (SWs) [1]. SWs are generated by a network of pacemaker cells named interstitial cells of Cajal (ICC) [2]. In the human stomach, SWs normally initiate and propagate at a frequency of approximately 3 cycles per minute (cpm) [3]. Impaired neuromuscular activity within the gut causes functional motility problems affecting more than 40% of the population worldwide [4].

Despite the high prevalence and impact on health care systems, the diagnosis of functional motility disorders is challenging and remains largely exclusionary [5]. Since slow wave events have a regulatory role in gastric motility, the analysis of SWs has potential for assessment of functional motility disorders. Moreover, degraded ICC networks and altered SW activity have been linked with functional motility disorders [6]-[8]. Some of these SW abnormalities include spatially-complex dysrhythmias that occur within the normal SW frequency range and cannot be identified using traditional frequency analysis techniques [7], [8].

High-resolution electrical mapping enables the analysis of SW propagation in spatio-temporal detail but the surgical invasiveness limits its clinical utility as a routine diagnostic method [9]. Hence, adopting slow-wave information in clinical practise has been challenging. Noninvasive electrogastrography (EGG) measurements using cutaneous electrodes [10], [11] are capable of capturing SW activity but the bioimpedance of body tissues limits the measurement of the low-amplitude gastric signals [12]. Hence, traditional EGG methods failed to provide clinical utility but recent use of multi-channel EGG systems and novel processing algorithms have allowed for detection of slow-wave propagation patterns [11], [13], [14].

Magnetic fields (MFs) generated by the gastric electric activity can also be reliably recorded via magnetogastrography (MGG) using superconducting quantum interference devices (SQUIDs) [15]. MGG provides higher signal to noise ratio (SNR) and a better resolution compared to EGG because MFs are not as greatly attenuated by muscle and fat layers. [16]. Hence, MGG can detect sources located deeper within the body and is a promising research

and potential diagnostic technique [17]. However, SQUIDs require super-cooling hardware and operate in magnetically shielded rooms, and therefore, they can be associated with high costs.

A number of studies have utilized MGG data to define the spatial features of SW activity [18], and a recent study showed that SW propagation parameters such as direction and speed can be extracted from MGG data [19]. However, the methods utilized in these studies constrained tracking of SWs to a plane defined by the sensor positions, and therefore identification of SW propagation in the antero-posterior direction was not feasible. On the other hand, source localization enables more accurate tracking and analysis of SW activity in three-dimensional (3D) space.

It has been previously reported that when the equivalent current dipole (ECD) model has been used to estimate the 3D distribution of SW activity in healthy humans, a characteristic migration of the estimated dipoles was observed across the stomach area [20]. Similarly, a single moving dipole model within one realistic homogeneous torso model was estimated from experimental MGG data and showed a good agreement with the stomach orientation [21].

Previous cardiac studies showed that biomagnetic fields measured outside the body can also be described by an equivalent magnetic dipole (EMD) moment [22], [23]. Moreover, the identified dipole moments and positions are shown to be correlated to the depolarization of cardiac tissues [24]. In a simulation study using realistic torso and stomach geometries of a single subject, a high correlation between the spatial trends of SWs and estimated dipole positions was reported when the EMD model was utilized to track SW propagation [25].

In this study, the ability of the ECD and EMD models to identify propagation details of SWs was investigated and compared using 4 anatomically realistic torso and stomach geometries and 2 types of simulated SW propagation patterns (antegrade and retrograde) with 2 types of rhythms (normogastric and bradygastric). Both methods were also applied to 2 human biomagnetic recordings to analyze propagation patterns in pre- and postprandial states.

II. Methods

The studies were approved by the Institutional Review Board at Vanderbilt University (Nashville, TN, USA) and all volunteers provided informed consent. Anatomically realistic torso and stomach geometries previously constructed from CT (computerized tomography) images of 4 healthy volunteers with varying body morphologies (Fig. 1) were used in this study [26]. In addition, two sets of experimental MGG data (pre- and postprandial) from one healthy volunteer were used to evaluate the proposed source localization methods. Experimental MGG data were acquired at 300 Hz and were digitally bandpass filtered (0.03-0.3 Hz) using a Butterworth filter in MATLAB R2019a (MathWorks Inc, Natick, MA, USA) for the subsequent analyses.

A. Electromagnetic Simulations

SW activation in the stomach was simulated using a finite element method, as previously described in [27], [28]. Two SW propagation patterns consistent with experimental observations in normal subjects and those with functional motility disorders and post-surgical dysmotility were studied: 1) antegrade propagation originating from the normal gastric pacemaker located on the greater curvature of the upper-corpus [3], and 2) retrograde propagation triggered by an ectopic pacemaker located in the distal antrum [7]. For each propagation pattern, we performed: (i) a bradygastric case with a frequency of < 1 cpm where only a single wavefront was present within the stomach at any given time, and (ii) a normogastric case with a 3 cpm activity where 2–4 wavefronts were always present. Hence, a total of 4 simulations were performed for each stomach and torso model.

The SW activity was represented by spatially and temporally varying stomach dipoles (SDPs) to bridge electrical and magnetic computations. The stomach models used in the simulations were defined using cubic Hermite mesh consisting of 64 elements and a single dipole per element was computed for each time point as follows:

$$\boldsymbol{\rho}_j = \frac{1}{S_j} \sum_{\xi=1}^{S_j} \nabla V_\xi \tag{1}$$

where $\boldsymbol{\rho}_j$ is the dipole vector computed for the j-th element (j = 1, …, 64), S_j is the number of solution points in j, and ∇V_ξ is the gradient of transmembrane potential at solution point ξ.

A total of 64 dipoles were computed for each time point representing the average activity within the elements. Dipole directions and positions were determined based on the strength of gradient vectors due to depolarization and repolarization, where depolarization vectors are generally larger than repolarization vectors due to higher potential difference between the solution points in the depolarization region.

Using dipoles as primary sources and the realistic torso models as the volume conductor, MF gradients were computed using the sensor positions and orientations of the SQUID array (Tristan Technologies, San Diego, CA, USA) located at Vanderbilt University (Fig. 1). Simulations were performed with a sampling frequency of 10 Hz using a continuum based simulation framework, CMISS (www.cmiss.org).

B. Source Localization

1) Forward Models: Let $\boldsymbol{B}(t)$ be a column vector ($n \times 1$) of MFs on n gradiometers (SQUID sensors) at time t. Then, $\boldsymbol{B}(t)$ can be expressed as a linear combination of a gain matrix $\boldsymbol{G}(t)$ and a dipole moment $\boldsymbol{\theta}(t)$

$$\boldsymbol{B}(t) = \boldsymbol{G}(t)\boldsymbol{\theta}(t), \tag{2}$$

where $\boldsymbol{G}(t)$ and $\boldsymbol{\theta}(t)$ have dimensions of $n \times 3$ and 3×1, respectively. The matrix representation of $\boldsymbol{B}(t)$ reduces the computational complexity of the source localization by separating the linear moment parameters from the location parameters [29]. The matrix $\boldsymbol{G}(t)$

is defined as a function of sensor locations and dipole position and is composed of kernel matrices as follows:

$$\boldsymbol{G}(t) = [\boldsymbol{K}_1(t)\boldsymbol{v}_1, \ldots, \boldsymbol{K}_n(t)\boldsymbol{v}_n], \tag{3}$$

where $\boldsymbol{K}_i(t)$ is the kernel matrix for the i-th sensor located at $\boldsymbol{r}_i$ and $\boldsymbol{v}_i$ is the direction vector between two coils in the gradiometer. The kernel matrices defined for the ECD and EMD models are summarized in the following sections.

Equivalent Current Dipole: The magnetic field $\boldsymbol{b}_i$ at a sensor point $\boldsymbol{r}_i$ due to a current dipole $\boldsymbol{q}$ in a homogeneous volume conductor located at $\boldsymbol{r}_q$ is given by [23]

$$\boldsymbol{b}_i(\boldsymbol{r}_i) = \frac{\mu_0}{4\pi}\left(\frac{\boldsymbol{q} \times \boldsymbol{d}_i}{d_i^3}\right), \tag{4}$$

where μ_0 is the permeability constant, $\boldsymbol{d}_i = \boldsymbol{r}_i - \boldsymbol{r}_q$ is the distance vector from the dipole to the observation point, and $d_i = \|\boldsymbol{d}_i\|_2$ is the L2 norm of $\boldsymbol{d}_i$.

The magnetic field $\boldsymbol{b}_i$ can also be represented as a product of a kernel matrix $\boldsymbol{K}_i$ and the dipole moment (i.e., $\boldsymbol{b}_i(\boldsymbol{r}_i) = \boldsymbol{K}_i(\boldsymbol{r}_i, \boldsymbol{r}_q)\boldsymbol{q}$). The kernel matrix can be computed using

$$\boldsymbol{K}_i(\boldsymbol{r}_i, \boldsymbol{r}_q) = \frac{\mu_0}{4\pi}\left(\frac{\boldsymbol{C}_{\boldsymbol{r}_q} - \boldsymbol{C}_{\boldsymbol{r}_i}}{d_i^3}\right), \tag{5}$$

where $\boldsymbol{K}_i$, $\boldsymbol{C}_{\boldsymbol{r}_q}$, and $\boldsymbol{C}_{\boldsymbol{r}_i}$ are each a 3 × 3 matrix as follows [29]:

$$\begin{aligned} \boldsymbol{C}_{\boldsymbol{r}_q} &= \begin{bmatrix} 0 & -\boldsymbol{r}_q(z) & \boldsymbol{r}_q(y) \\ \boldsymbol{r}_q(z) & 0 & -\boldsymbol{r}_q(x) \\ -\boldsymbol{r}_q(y) & \boldsymbol{r}_q(x) & 0 \end{bmatrix} \\ \boldsymbol{C}_{\boldsymbol{r}_i} &= \begin{bmatrix} 0 & -\boldsymbol{r}_i(z) & \boldsymbol{r}_i(y) \\ \boldsymbol{r}_i(z) & 0 & -\boldsymbol{r}_i(x) \\ -\boldsymbol{r}_i(y) & \boldsymbol{r}_i(x) & 0 \end{bmatrix} \end{aligned} \tag{6}$$

Equivalent Magnetic Dipole: The magnetic field $\boldsymbol{b}_i$ at a sensor point $\boldsymbol{r}_i$ generated by a magnetic dipole moment $\boldsymbol{m}$ in a homogeneous volume conductor located at $\boldsymbol{r}_m$ is defined by

$$\boldsymbol{b}_i(\boldsymbol{r}_i) = \frac{\mu_0}{4\pi}\left(\frac{3\boldsymbol{d}_i(\boldsymbol{m}\boldsymbol{d}_i)}{d_i^5} - \frac{\boldsymbol{m}}{d_i^3}\right), \tag{7}$$

where $\boldsymbol{d}_i = \boldsymbol{r}_i - \boldsymbol{r}_m$ [23]. Similar to the ECD, $\boldsymbol{b}_i$ can be expressed as a product of kernel matrix and dipole moment (i.e., $\boldsymbol{b}_i(\boldsymbol{r}_i) = \boldsymbol{K}_i(\boldsymbol{r}_i, \boldsymbol{r}_m)\boldsymbol{m}$), and the equation of the kernel matrix $\boldsymbol{K}_i$ corresponds to

$$\boldsymbol{K}_i(\boldsymbol{r}_i, \boldsymbol{r}_m) = \frac{\mu_0}{4\pi}\left(\frac{3(\boldsymbol{d}_i\boldsymbol{d}_i^T)\boldsymbol{I}}{d_i^5} - \frac{\boldsymbol{I}}{d_i^3}\right), \tag{8}$$

where $\boldsymbol{I}$ is the 3 × 3 identity matrix.

2) Inverse Solution: For a set of MF gradients $\boldsymbol{B}(t)$, unbiased estimates of $\boldsymbol{\theta}(t)$ and $\boldsymbol{r}_\theta(t)$ (denoted as $\hat{\boldsymbol{\theta}}(t)$ and $\hat{\boldsymbol{r}}_\theta(t)$, respectively) can be obtained using maximum likelihood estimate [30], by minimizing the following objective function:

$$f(\boldsymbol{r}_\theta) = \mathrm{tr}\left\{(\boldsymbol{I} - \boldsymbol{G}(\boldsymbol{G}^T\boldsymbol{G})^{-1}\boldsymbol{G}^T)\hat{\boldsymbol{R}}\right\}, \tag{9}$$

where tr{·} is the trace operator and $\hat{\boldsymbol{R}}$ is the estimate of the covariance matrix obtained from $\boldsymbol{B}$. Then, $\hat{\boldsymbol{r}}_\theta$ is given by the following formula:

$$\hat{\boldsymbol{r}}_\theta = \arg\min_{\boldsymbol{r}_\theta} f(\boldsymbol{r}_\theta)\,. \tag{10}$$

Once source localization converged to the best-fitted $\hat{\boldsymbol{r}}_\theta$ using the Nelder-Mead simplex method, the dipole moment can be obtained using least-squares fit:

$$\hat{\boldsymbol{\theta}} = (\hat{\boldsymbol{G}}^T\hat{\boldsymbol{G}})^{-1}\hat{\boldsymbol{G}}^T\boldsymbol{B}, \tag{11}$$

where $\hat{\boldsymbol{G}}$ is the estimated gain matrix due to $\hat{\boldsymbol{r}}_\theta$ computed using (3) and T is the transpose operator. Then, $\hat{\boldsymbol{B}}$ can be forward-computed using $\hat{\boldsymbol{\theta}}$ and $\hat{\boldsymbol{r}}_{\boldsymbol{\theta}}$ using (2).

C. Analytical Metrics

1) Goodness-of-fit: The goodness-of-fit (GOF) was used to assess how well the estimated dipoles ($\hat{\boldsymbol{m}}$ and $\hat{\boldsymbol{q}}$) described the MFs ($\boldsymbol{B}$) by comparing against the forward-computed MFs ($\hat{\boldsymbol{B}}$) as follows:

$$GOF = \frac{\|\boldsymbol{B}\|_2 - \|\boldsymbol{B} - \hat{\boldsymbol{B}}\|_2}{\|\boldsymbol{B}\|_2}\,. \tag{12}$$

GOF values were expressed as percentage, and if $\|\boldsymbol{B} - \hat{\boldsymbol{B}}\|_2 > \|\boldsymbol{B}\|_2$, then the source localization was considered to have failed and the GOF was set to zero.

2) Pattern Analysis: The concordance between the estimated magnetic/current dipole positions and SW activity was assessed by using the SDPs ($\boldsymbol{\rho}$) that were responsible for generating the MFs. First, the mean (weighted-average) position of SDPs ($\boldsymbol{r}_{\rho,c}$) at time t was computed by

$$\boldsymbol{r}_{\rho,c}(t) = \frac{\sum_{k=1}^{n}\boldsymbol{r}_{\rho,k}\|\boldsymbol{\rho}_k\|_2}{\sum_{k=1}^{n}\|\boldsymbol{\rho}_k\|_2}, \tag{13}$$

where $\boldsymbol{\rho}_k$ corresponds to the k-th SDP located at $\boldsymbol{r}_{\rho,k}$. Then, $\hat{\boldsymbol{r}}_q(t)$ and $\hat{\boldsymbol{r}}_m(t)$ were compared against $\boldsymbol{r}_{\rho,c}(t)$ by computing the distances and the Pearson correlation coefficients for spatial patterns in the lateral (x-axis), antero-posterior (y-axis), and supero-inferior (z-axis) axes.

The propagation patterns were also analyzed by computing the azimuth and elevation between $\hat{\boldsymbol{r}}_m(t)$ and $\hat{\boldsymbol{r}}_m(t+1)$, and between $\hat{\boldsymbol{r}}_q(t)$ and $\hat{\boldsymbol{r}}_q(t+1)$. Azimuth was used to identify the propagation in the antero-posterior axis whereas elevation revealed any propagation profile in the supero-inferior axis.

3) Impact of Noise: The impact of different noise levels on source localization was assessed by comparing the distances of the ECD and EMD from the mean SDP position, correlation coefficients, and GOFs after two levels of white noise were added to the MF data resulting in SNRs of 20 dB and 10 dB, respectively. This process was repeated 30 times for each data set and the median distance, correlation coefficient, and GOF values were computed.

4) Statistical Comparison: The localization results of the ECD and EMD models were compared via Wilcoxon rank-sum test with a significance level (alpha) of 0.05 using MATLAB R2019a (MathWorks Inc, Natick, MA, USA). Data were expressed as median (IQR - interquartile range).

III. Results

A. Simulation Data

Simulations in all stomach geometries achieved realistic normal (antegrade) and ectopic (retrograde) propagation patterns with either a bradygastric (< 1 cpm) or normal (3 cpm) rhythm, as observed in previous experimental studies of healthy, diseased, and post-surgical patients [7], [8]. MF simulations reflected these SW frequencies as displayed in Fig. 2, where one MF trace from bradygastric and normogastric simulations was displayed together with an experimental MF trace. All traces corresponded to the same sensor and were temporarily aligned based on the first peak. The amplitudes of each trace were normalized for visualization purposes only. The MF obtained from the normogastric simulation was in good agreement with the experimental data.

Source localization in all cases was performed for a time period between two MF peaks (approximately 60 s for the bradygastric simulations and 20 s for normogastric simulations and experimental data). Therefore, bradygastric simulations resulted in three times more localization results than normogastric simulations and experimental data. A representative source localization outcome from a bradygastric simulation is illustrated in Fig. 3. Only one wavefront was present in the stomach for this time point as shown in Fig. 3(a). The 8 SDPs within the elements where the wavefront was located are displayed in Fig. 3(b-c). These dipoles were oriented in the direction of propagation since the gradient vectors of transmembrane potential in the leading edge of the wavefront due to depolarization were larger than the gradient vectors of the repolarization in the trailing edge. The remaining 56 SDPs computed for the elements without a slow wave activity only reflected by variations in the resting membrane potential gradient. Therefore, they were approximately 200 times

smaller than the dipoles due to the SW activity and were not displayed in Fig. 3(b-c). As expected, the mean SDP position displayed as an orange sphere was located in the middle of SDPs, and the ECD position (blue sphere) and the EMD position (green sphere) were in the vicinity of the SDPs. As seen in Fig. 3(b-c), the ECD was closer to the mean SDP position compared to the EMD (distance: 11.7 vs 31.4 mm). The resultant MF distribution due to the SW exhibited a bipolar pattern within the coverage of the sensor array as depicted in Fig. 3(d). The field distributions due to the EMD (Fig. 3(e)) and the ECD (Fig. 3(f)) had similar bipolar patterns but the MF distribution due to the EMD was more agreement with the resultant MF of the SW activity. The EMD more extensively described the MFs than the ECD (GOF: 86.6% vs 76.5%) for this particular case.

Table I summarizes the GOF and distance results for the ECD and EMD obtained from all bradygastric and normogastric simulations. The EMD achieved higher GOFs in both bradygastric simulations (median: 90.7% vs 69.5%, $P<0.001$) and normogastric simulations (median: 90.1% vs 67.5%, $P<0.001$) suggesting a better description of MFs. On the other hand, the ECD was closer to the mean SDP position with the median distances of 15.5 vs 28.9 mm ($P<0.001$) in bradygastric simulations and 20.2 vs 32.3 mm ($P<0.001$) in normogastric simulations. In addition, GOF values for both EMD and ECD models did not show a large difference in bradygastric vs normogastric simulations, whereas their distance to the mean SDP position increased by around 3–5 mm in the normogastric simulations compared to those is in the bradygastric simulations (Table I).

Although the EMD model produced larger distances with respect to the mean SDP position, it outperformed the ECD model in tracking overall SW propagation pattern and resulted in larger correlations in all axes. The correlation coefficients between mean SDP and source localization results for the bradygastric and normogastric simulations are illustrated in Fig. 4(a) and Fig. 4(b), respectively. Each boxplot corresponds to the distribution of 8 correlation coefficients obtained from 4 geometries (one for antegrade and one for retrograde propagation). The SW propagation in the lateral (x-axis) and supero-inferior (z-axis) directions were extensively captured by the EMD model producing median correlation coefficients >0.9 for the bradygastric simulations. The model was capable of detecting the propagation in the antero-posterior (y-axis) direction with a median correlation of 0.68 (0.57–0.80). On the other hand, the ECD model produced lower correlation scores with greater variation. The median correlation coefficients between the SW activity and the ECD model in x-, y-, and z-axis were 0.08, 0.27, and 0.12 lower than those of the EMD model, respectively.

The concordance between the estimated ECD and EMD positions and the mean SDP position was lower in normogastric simulations but the EMD model was still capable of identifying the SW propagation in x-, y-, and z-directions with median correlation coefficients of 0.66 (0.55–0.76), 0.53 (0.44–0.81), and 0.83 (0.72–0.91), respectively. Similar to the bradygastric simulations, the correlations obtained by the ECD model were lower than those of the EMD model with a median value around 0.5.

Source localization using the EMD model was more robust to noise conditions. Even though GOF values dropped by approximately 10% in the bradygastric simulations and 15% in

normogastric simulations from the noiseless case to the noise level with an SNR of 10 dB, the localized EMD positions were largely stable. The change in the median Euclidean distance from the estimated EMD position to the mean SDP position was almost negligible for the EMD model in both bradygastric and normogastric simulations (Table I). Therefore, the correlation scores in all directions did not change significantly, but there was still a decrease especially when the SNR of the data was 10 dB (Fig. 4). The reduction in correlation scores with noise was larger for the ECD model and the correlation coefficients dropped to 0.3 in the x- and z-axis and 0.2 in the y-axis.

In order to reveal propagation signatures of antegrade and retrograde SW patterns, the propagation of the EMD and ECD positions over time were analyzed by computing the azimuth and elevation between the displacement vector of the estimated EMD and ECD positions in two successive time points. Fig. 5 displays the polar histograms for the antegrade and retrograde patterns in normogastric simulations together with experimental MGG data.

For the antegrade propagation (Fig. 5(a)), the angles of between two successive EMD positions were largely in the third quadrant in the supero-inferior axis suggesting a propagation from top to bottom and largely from left to right. In the antero-posterior axis, the range of dominant angles was larger indicating propagation towards anterior surface to right-posterior region. The distribution of the angles obtained from the ECD model in antegrade simulations had a wider range than the EMD model and the dominant angles largely indicated a migration in the right-superior and right-anterior directions.

For the retrograde simulations (Fig. 5(b)), the angles in the supero-inferior axis, resulted by the EMD model were mostly in the first quadrant indicating a propagation in the left-superior direction. However, this behaviour was not prominent in the ECD model since it produced angles almost equally in the first, third and forth quadrants. The behaviour of both models in the antero-posterior axis was more alike producing angles largely in the first and forth quadrants suggesting a migration towards left-posterior surface.

B. Experimental Data

When MGG recordings were used in the source localization and pre- and postprandial results were pooled, the EMD model showed a narrower range where most of the angles were in the third quadrant for the supero-inferior and antero-posterior axes (Fig. 5(c)). However, the ECD model resulted in two clusters of angles oriented in the superior and inferior directions. In the postero-anterior axis, the majority of the angles indicated a dominant propagation towards the right.

The spatial signatures obtained using the EMD model were comparable for both the pre- and postprandial data where antegrade-like signatures were observed. The EMD propagation patterns in the both pre- and postprandial recordings resulted in angles largely in the third quadrants with a ratio of 49% in both the supero-inferior and antero-posterior axes for the preprandial data. Similarly, the postprandial data had angles mostly within the third quadrant with the ratios of 35% and 50% in the supero-inferior and antero-posterior axes,

respectively. The ratio of angles in the third quadrant dropped 14% in the postprandial recording due to the increased activity toward the right-superior direction.

For the preprandial recording, the ECD model resulted in angles mostly in the second and third quadrants with a similar percentages around 30% while a substantial amount of angles were also observed in the first (20%) and forth (15%) quadrants in the both supero-inferior and antero-posterior directions. The postprandial data showed similar signatures with 1%-4% changes in all quadrants in the supero-inferior direction. However, the postprandial activity in the antero-posterior direction resulted in increased angles in the second and third quadrants with a total of 70% of all angles.

IV. Discussion

In this study, SWs and MFs were simulated using anatomically realistic stomach and torso geometries of four subjects. The use of the EMD and ECD models to characterize the spatial signatures of SW activity was investigated. The source localization performance of both models and their ability to track SW patterns were quantified and compared under three noise levels. In addition, the propagation of the estimated EMD and ECD positions over time was analyzed to reveal the propagation signatures of the simulated data.

The simulated data aimed to test source localization performance in two scenarios where only one or multiple slow wave events were observed in the stomach at any given time. Therefore, an extreme form of bradygastria was chosen to achieve the one wave scenario while normogastric case was performed for the multiple-wave scenario. The EMD and ECD models were then applied to two experimental MGG data sets to validate the approach of source localisation. The simulation and experimental results demonstrated that the EMD model outperformed the ECD model for source localization of gastric SW activity and could provide a promising and valuable technique for analyzing SW propagation.

The simulated SW propagation patterns (antegrade and retrograde) and rhythms (normal and bradygastric) were consistent with the experimental observations, and more importantly, the dysrhythmic patterns and frequencies have been linked with functional motility disorders [3], [7], [8]. However, it is critically important to extensively represent the SW activity in MF simulations. Most of the earlier simulation studies used either moving current dipole models [18] to mimic SW propagation patterns or simulated SWs represented by a single dipole [26] to simulate MFs. In this study, multiple stomach dipoles were computed from the simulated membrane potentials and used as the primary sources to bridge SW potentials with MF computations. In addition, the contribution of secondary sources from realistic torso models was included. Hence, our simulated MFs were in good agreement with the experimental data as seen in Fig. 2.

Source localization of SW activity was performed using the ECD and EMD models. The ECD model has been widely utilized in source localization of biomagnetic fields [31], [32] whereas the EMD model has been mostly used in cardiac studies to represent the biomagnetic data [22], [23]. Since the higher-order components of MFs are not usually observed in MF measurements as they drop-off with distance more rapidly, the ECD and

EMD models are expected to sufficiently explain biomagnetic data [33]. Our GOF results showed that the EMD model extensively described the simulated MFs in both bradygastric and normogastric simulations, being approximately 20–25% higher than the ECD model in all noise levels. Although having high GOF values usually implies better source localization performance, the inverse solutions are known to be ill-posed and cannot be uniquely solved because the same field distribution can be produced by other source configurations as well [34]. Moreover, using GOF to compare the localization performance of different models (ECD vs EMD) could be misleading, as shown by our results where the ECD model resulted in lower GOFs but achieved closer estimation to the mean SDP position.

One of the important findings in this study is that even though the EMD positions were approximately 15 mm more distant to the mean SDP position, its ability to represent SW propagation trajectory was higher compared to the ECD model, as quantified by the correlation coefficients in x-, y-, and z-directions. It was previously shown that the EMD model can track SW propagation with a high correlation when anatomically realistic torso and stomach geometries of a single subject and a hypothetical high-density and high-coverage MGG array were used [25]. Our findings in this study further show that the EMD model is capable of estimating overall SW trajectory in various anatomies using the experimental MGG sensor layout with a correlation score of > 0.5 for all noise levels, even in normogastric simulations with multiple existing wavefronts. The ECD model, on the other hand, has greater variation and lower correlation scores, suggesting that it is more likely to fail to follow the trajectory of the SW activity, even if it was often located closer to the mean SDP (Table I).

The poorer performance of the ECD model was expected as the ECD model usually performs better when it is used with a volume conductor model since the contribution of conducting volume accounts for 30%–50% of the magnetic fields outside the volume [35], [36]. On the other hand, the EMD model has been reported as a good representation of underlying sources without needing a volume conductor [22], [23]. Two earlier studies performed on the same experimental magnetocardiographic data showed that the ECD model alone was inaccurate in estimating the source dynamics, but a realistic torso model provided more accurate representation [23], [37]. More importantly, the findings in these studies showed that the EMD model was capable of localizing the underlying sources as accurately as the ECD model with a volume conductor [23], [37].

The polar analysis of the EMD positions performed on normogastric simulations showed a directionality consistent with SW propagation and stomach curvatures and orientations. Source localization also enables analysis of the propagation patterns in the antero-posterior axis. Similar to the angles in the supero-inferior axis, there were characteristic and opposite signatures for both antegrade and retrograde simulations in the antero-posterior axis when the EMD model was used. On the other hand, the spatial signatures of the ECD model did not reflect the actual propagation trajectories as extensively as the EMD model.

The spatial signatures of the EMD model were in close agreement with previous experimental findings, further supporting the accuracy and validity of the model. Similar spatial propagation results were previously reported by a study using experimental MGG

data where control subjects exhibited left to right patterns while gastroparesis patients showed either deviations from the normal pattern or a completely opposite right to left propagation [19]. Gastroparesis patients were previously associated with retrograde propagation identified using intraoperative high-resolution serosal mapping [7]. Similarly, the signatures of the EMD model were in agreement with the findings obtained from the EGG recordings of control, functional dyspepsia and gastroparesis subjects [11].

The EMD model also yielded more meaningful results for the experimental MGG data where normal-like propagation signatures similar to the antegrade simulation results were observed. These results (normal antegrade propagation) are expected to be observed in these MGG recordings as the volunteer had no reported gastric motility problems. The results obtained from the ECD model were less expected as it generated two opposite directions of propagation patterns in the supero-inferior direction. Such an observation might be real and meaningful as well implying an unstable SW propagation, however, it is unlikely to have happened for this data within a time-span of one wavefront. Hence, simulation and experimental results clearly show that the EMD model outperforms the ECD model and source localization using the EMD model could be a promising technique of analyzing spatial patterns of SW propagation.

Despite all the evidence showing a good agreement between this simulation-based work and experimental observations, there were a number of limitations worth noting. Firstly, the homogeneous volume conductor model used in this study may have underestimated the contribution of secondary sources, even though this is a common simplification in biomagnetic simulation studies [38], [39]. In addition, environmental noise was assumed to be Gaussian and no contribution from external interference or other bioelectric sources was incorporated in the MF simulations. However, external noise sources are unlikely to significantly impact experimental MGG data because magnetic shielding can reduce the noise level to as low as 1 $fT / \sqrt{Hz}$ [40]. Additionally, bioelectric sources not originating from the stomach can be efficiently removed from the gastric data using filtering and source separation techniques due to the distinct frequency profiles and locations of each source [19]. Finally, the deterministic Nelder-Mead simplex method was used to estimate the optimum values with very low computational cost. Probabilistic and evolutionary optimization strategies may improve the source localization with low SNR conditions or high-dimensional search space.

This simulation-based approach managed to accurately quantify and evaluate localization performance and verified the ability of the ECD and EMD models to estimate SW propagation trajectory as ground-truth knowledge of the underlying SW activity was available. Although four subject-specific anatomically realistic geometries were assumed to provide enough anatomical variation and to be sufficient to identify broad trends in the performance of source localization, further investigations using a larger cohort would yield more robust results. More importantly, simulations of a range of additional realistic SW propagation patterns linked with functional motility disorders such as conduction blocks, re-entry, ectopic pacemakers, and tachygastric rhythm, would enable identification of the spatial signatures of such propagation types and would enhance existing diagnostic methods. Extracting these signatures using experimental data would not be feasible in human patients

as it requires simultaneous measurement of MGG and the underlying SW activity using invasive high-resolution mapping. There is also a need for more extensive experimental analysis to validate the efficacy of the source localization.

V. Conclusion

This study identified and compared the ability of the EMD and ECD models to characterize the spatial signatures of gastric electrical activity. Our study has provided evidence that the EMD model outperformed the ECD model in tracking the SW propagation patterns. More importantly, the EMD model was shown to be a promising means to identify and classify the spatial signatures of SW activities, which can provide a valuable non-invasive tool for investigating the growing field of bioelectrical SW dysrhythmias in functional motility disorders and post-surgical dysmotility, potentially contributing to improved diagnosis methods.

Acknowledgments

The work was funded, in part, by National Institutes of Health (R01 HD088662), Marsden Fund Council, Health Research Council of New Zealand, Medical Technologies Centre of Research Excellence (MedTech CoRE), and Riddet Institute. CEE was supported by a University of Auckland Doctoral Scholarship. PD and TRA-G were supported by Rutherford Discovery Fellowships from the Royal Society Te Apārangi.

References

[1]. Cooke AR, “Control of gastric emptying and motility.” Gastroenterology, vol. 68, no. 4 Pt 1, pp. 804–16, 1975. [PubMed: 1123145]

[2]. Huizinga JD and Lammers WJEP, “Gut peristalsis is governed by a multitude of cooperating mechanisms.” Am J Physiol - Gastrointest Liver Physiol, vol. 296, no. 1, pp. G1–8, 2009. [PubMed: 18988693]

[3]. O’Grady G, et al. , “Origin and propagation of human gastric slow-wave activity defined by high-resolution mapping.” Am J Physiol - Gastrointest Liver Physiol, vol. 299, no. 3, pp. g585–92, 2010. [PubMed: 20595620]

[4]. Sperber AD, et al. , “Worldwide prevalence and burden of functional gastrointestinal disorders, results of Rome Foundation global study,” Gastroenterology, vol. 160, no. 1, pp. 99–114, 2021. [PubMed: 32294476]

[5]. Avci R, et al. , “Bioelectrical Signals for the Diagnosis and Therapy of Functional Gastrointestinal Disorders,” Appl Sci, vol. 10, no. 22, p. 8102, 2020.

[6]. Grover M, et al. , “Cellular changes in diabetic and idiopathic gastroparesis.” Gastroenterology, vol. 140, no. 5, pp. 1575–85.e8, 2011. [PubMed: 21300066]

[7]. O’Grady G, et al. , “Abnormal initiation and conduction of slow-wave activity in gastroparesis, defined by high-resolution electrical mapping.” Gastroenterology, vol. 143, no. 3, pp. 589–98.e1–3, 2012. [PubMed: 22643349]

[8]. Angeli TR, et al. , “Loss of interstitial cells of Cajal and patterns of gastric dysrhythmia in patients with chronic unexplained nausea and vomiting.” Gastroenterology, vol. 149, no. 1, pp. 56–66.e5, 2015. [PubMed: 25863217]

[9]. Du P, et al. , “High-resolution mapping of in vivo gastrointestinal slow wave activity using flexible printed circuit board electrodes: Methodology and validation,” Ann Biomed Eng, vol. 37, no. 4, pp. 839–846, 2009. [PubMed: 19224368]

[10]. Koch KL, “Gastric dysrhythmias: a potential objective measure of nausea.” Exp Brain Res, vol. 232, no. 8, pp. 2553–61, 2014. [PubMed: 24916149]

[11]. Gharibans AA, et al. , “Spatial Patterns From High-Resolution Electrogastrography Correlate With Severity of Symptoms in Patients With Functional Dyspepsia and Gastroparesis.” Clin Gastroenterol Hepatol, vol. 17, no. 13, pp. 2668–2677, 2019. [PubMed: 31009794]

[12]. Bradshaw LA, et al. , “Volume conductor effects on the spatial resolution of magnetic fields and electric potentials from gastrointestinal electrical activity.” Med Biol Eng Comput, vol. 39, no. 1, pp. 35–43, 2001. [PubMed: 11214271]

[13]. Mika B, et al. , “Empirical mode decomposition for slow wave extraction from electrogastrographical signals,” Annu Int Conf IEEE Eng Med Biol Soc, vol. 2015, pp. 4138–4141, 2015. [PubMed: 26737205]

[14]. Mika B, et al. , “Assessment of slow wave propagation in multichannel electrogastrography by using noise-assisted multivariate empirical mode decomposition and cross-covariance analysis,” Comput Biol Med, vol. 100, pp. 305–315, 2018. [PubMed: 29397919]

[15]. Bradshaw LA, et al. , “Biomagnetic characterization of spatiotemporal parameters of the gastric slow wave.” Neurogastroenterol Motil, vol. 18, no. 8, pp. 619–31, 2006. [PubMed: 16918726]

[16]. Somarajan S, et al. , “Effects of body mass index on gastric slow wave: A magnetogastrographic study,” Physiol Meas, vol. 35, no. 2, p. 205, 2014. [PubMed: 24398454]

[17]. Kim JHK, et al. , “Influence of body parameters on gastric bioelectric and biomagnetic fields in a realistic volume conductor.” Physiol Meas, vol. 33, no. 4, pp. 545–56, 2012. [PubMed: 22415019]

[18]. Bradshaw LA, et al. , “Surface current density mapping for identification of gastric slow wave propagation.” IEEE Trans Biomed Eng, vol. 56, no. 8, pp. 2131–9, 2009. [PubMed: 19403355]

[19]. Bradshaw LA, et al. , “Diabetic gastroparesis alters the biomagnetic signature of the gastric slow wave.” Neurogastroenterol Motil, vol. 28, no. 6, pp. 837–48, 2016. [PubMed: 26839980]

[20]. Allescher HD, et al. , “Biomagnetic 3-dimensional spatial and temporal characterization of electrical activity of human stomach.” Dig Dis Sci, vol. 43, no. 4, pp. 683–93, 1998. [PubMed: 9558020]

[21]. Cheng LK, et al. , “Noninvasive Localization of Gastric Electrical Activity,” Int J Bioelectromagn, vol. 7, no. 1, pp. 1–4, 2005.

[22]. Karp PJ, et al. , “The normal human magnetocardiogram. II. A multipole analysis.” Circ Res, vol. 47, no. 1, pp. 117–130, 1980. [PubMed: 7379262]

[23]. Nenonen J, et al. , “Magnetocardiographic functional localization using current multipole models.” IEEE Trans Biomed Eng, vol. 38, no. 7, pp. 648–57, 1991. [PubMed: 1879857]

[24]. Avci R, et al. , “Tracking fetal movement through source localization from multisensor magnetocardiographic recordings,” IEEE J Biomed Heal Informatics, vol. 22, no. 3, pp. 758–765, 2018.

[25]. Avci R, et al. , “Source localization for gastric electrical activity using simulated magnetogastrographic data.” Annu Int Conf IEEE Eng Med Biol Soc, vol. 2019, pp. 2336–2339, 2019. [PubMed: 31946368]

[26]. Komuro R, et al. , “Comparison and analysis of inter-subject variability of simulated magnetic activity generated from gastric electrical activity.” Ann Biomed Eng, vol. 36, no. 6, pp. 1049–59, 2008. [PubMed: 18330701]

[27]. Buist ML, et al. , “An anatomical model of the gastric system for producing bioelectric and biomagnetic fields.” Physiol Meas, vol. 25, no. 4, pp. 849–61, 2004. [PubMed: 15382826]

[28]. Eichler CE, et al. , “Effects of magnetogastrography sensor configurations in tracking slow wave propagation,” Comput Biol Med, p. 104169, 2020. [PubMed: 33338892]

[29]. Mosher J, et al. , “EEG and MEG: forward solutions for inverse methods,” IEEE Trans Biomed Eng, vol. 46, no. 3, pp. 245–259, 1999. [PubMed: 10097460]

[30]. Stoica P and Nehorai A, “MUSIC, maximum likelihood, and Cramer-Rao bound,” IEEE Trans Acoust, vol. 37, no. 5, pp. 720–741, 1989.

[31]. Pesola K, et al. , “Multichannel magnetocardiographic measurements with a physical thorax phantom,” Med Biol Eng Comput, vol. 37, no. 1, pp. 2–7, 1999. [PubMed: 10396834]

[32]. He B, et al. , “Electrophysiological Source Imaging: A Noninvasive Window to Brain Dynamics,” Annu Rev Biomed Eng, vol. 20, no. 1, pp. 171–196, 2018. [PubMed: 29494213]

[33]. Malmivuo J and Plonsey R, Bioelectromagnetism: Principles and Applications of Bioelectric and Biomagnetic Fields. Oxford University Press, 1995.

[34]. Baillet S, et al. , “Electromagnetic brain mapping,” IEEE Signal Process Mag, vol. 18, no. 6, pp. 14–30, 2001.

[35]. Hosaka H, et al. , “Part III: the effect of the torso boundaries on the magnetocardiogram.” J Electrocardiol, vol. 9, no. 4, pp. 418–25, 1976. [PubMed: 978095]

[36]. Komuro R, et al. , “Effects of volume conductor and source configuration on simulated magnetogastrograms,” Phys Med Biol, vol. 55, no. 22, pp. 6881–6895, 2010. [PubMed: 21048291]

[37]. Nenonen J, et al. , “Magnetocardiographic functional localization using a current dipole in a realistic torso.” IEEE Trans Biomed Eng, vol. 38, no. 7, pp. 658–64, 1991. [PubMed: 1879858]

[38]. Hämäläinen MS and Sarvas J, “Realistic conductivity geometry model of the human head for interpretation of neuromagnetic data.” IEEE Trans Biomed Eng, vol. 36, no. 2, pp. 165–71, 1989. [PubMed: 2917762]

[39]. Cuffin BN and Geselowitz DB, “Computer model studies of the magnetocardiogram,” Ann Biomed Eng, vol. 5, no. 2, pp. 164–178, 1977. [PubMed: 883701]

[40]. Körber R, et al. , “SQUIDs in biomagnetism: A roadmap towards improved healthcare,” Supercond Sci Technol, vol. 29, no. 11, 2016.

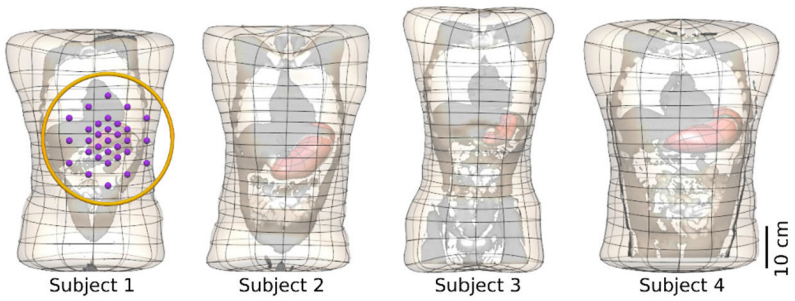

Fig. 1:

Stomach and torso geometries used in slow wave and magnetic dipole simulations overlaid with a computerized tomography image in the coronal plane. The sensor layout used in the simulations is shown with purple spheres on Subject 1.

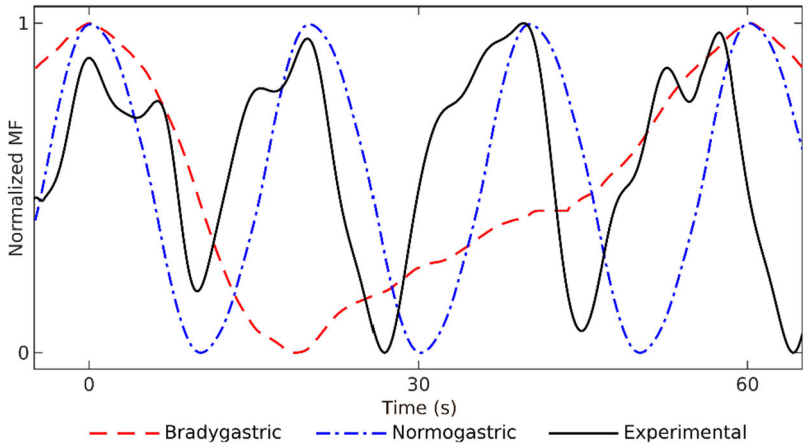

Fig. 2:

Representative magnetic field traces of bradygastric (red) and normogastric (blue) simulations together with an experimental magnetic field trace (black). The peaks of all three field traces were aligned at 0 s and displayed for a period of 60 s. The amplitudes of each trace were normalized for visualization purposes only.

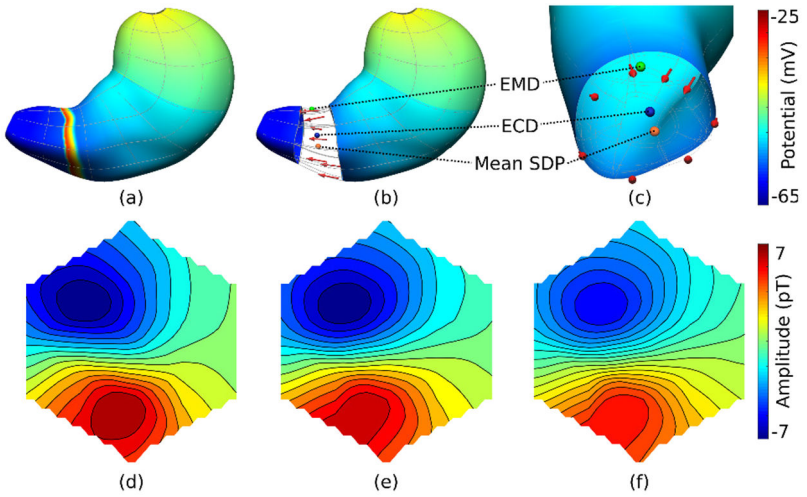

Fig. 3:

A representative source localization result for a bradygastric simulation. The membrane potentials are shown in (a) where only one wavefront exists. The stomach dipoles (SDPs) within the 8 elements containing the wavefront are displayed in (b) and (c) together with the mean SDP position (orange sphere), the equivalent current dipole (ECD) position (blue sphere) and the equivalent magnetic dipole (EMD) position (green sphere). Magnetic field vectors over the sensors due to (d) the slow wave activity, (e) the EMD, and (f) the ECD are shown.

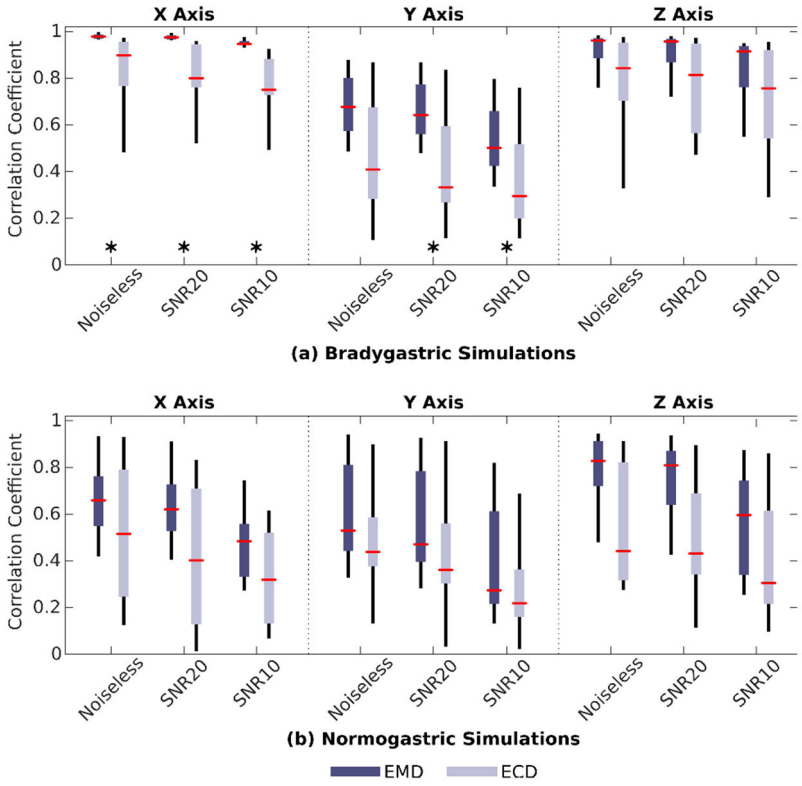

Fig. 4:

The correlation coefficients between stomach dipoles and source localization results (N = 8). Bradygastric and normogastric simulation results under three different noise conditions are summarized and compared in (a) and (b), respectively. (* P<0.05)

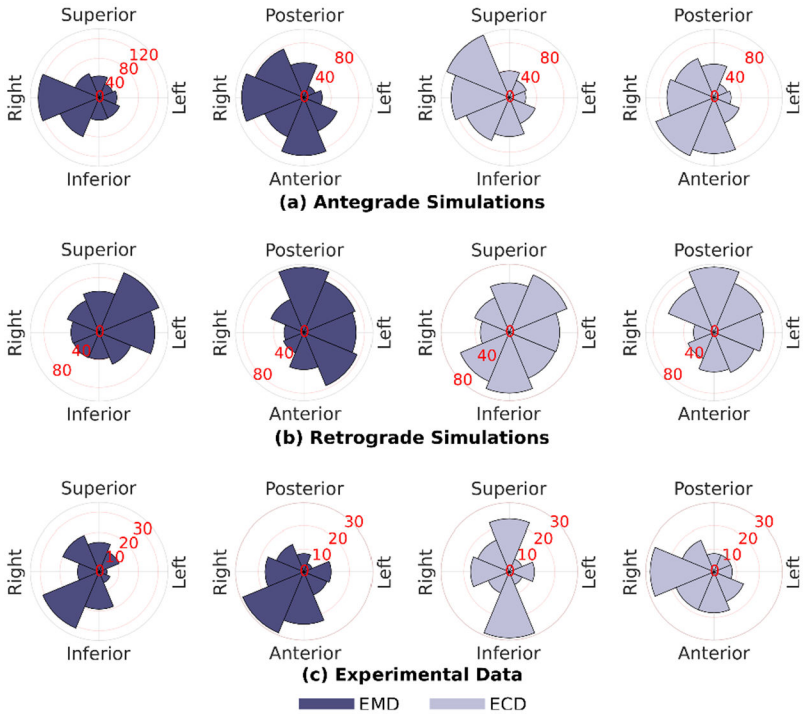

Fig. 5:

Polar histograms depicting the distribution of propagation directions of the equivalent magnetic dipole (EMD) and equivalent current dipole (ECD) positions in normogastric noise-free simulations and experimental magnetogastrography (MGG) data. (a) the antegrade simulations, (b) retrograde simulations, and (c) experimental MGG.

TABLE I:

Descriptive statistics of goodness-of-fit (GOF) and distance metrics for the equivalent magnetic dipole (EMD) and equivalent current dipole (ECD) models (N = 8).

			EMD	ECD	P
Bradygastric	**GOF (%)**	Noiseless	90.7 (90.1 – 93.5)	69.5 (60.8 – 77.2)	< **0.001**
		SNR20	88.8 (87.8 – 90.8)	68.3 (60.3 – 75.9)	< **0.001**
		SNR10	78.7 (77.0 – 79.6)	63.2 (56.2 – 68.6)	< **0.001**
	Distance (mm)	Noiseless	28.9 (23.2 – 31.5)	15.5 (9.3 – 17.9)	< **0.001**
		SNR20	28.9 (23.3 – 31.5)	16.2 (10.8 – 17.3)	< **0.001**
		SNR10	29.0 (23.5 – 31.8)	17.4 (11.9 – 18.3)	**0.001**
Normogastric	**GOF (%)**	Noiseless	90.1 (89.9 – 92.3)	67.5 (58.9 – 75.6)	< **0.001**
		SNR20	87.3 (86.5 – 89.0)	66.4 (58.5 – 74.1)	< **0.001**
		SNR10	74.4 (71.9 – 75.6)	60.5 (53.8 – 65.4)	< **0.001**
	Distance (mm)	Noiseless	32.3 (24.9 – 44.6)	20.2 (12.3 – 32.0)	**0.038**
		SNR20	32.3 (25.0 – 44.7)	21.1 (12.6 – 31.4)	0.065
		SNR10	32.8 (25.3 – 45.2)	22.9 (14.7 – 31.3)	0.083

IEEE Trans Biomed Eng. Author manuscript; available in PMC 2023 November 01.